NUCLEATION PROCESS IN ASYMMETRIC NUCLEAR MATTER

D.P.Menezes * *and C. Providência*

Centro de Física Teórica - Depto de Física - Universidade de Coimbra

3000 - Portugal

* *Permanent Address: Depto de Física - CFM - Universidade Federal de Santa Catarina*

Florianópolis - SC - CP. 476 - CEP 88.040 - 900 - Brazil

Abstract

An extended version of the non linear Walecka model, with ρ mesons and eletromagnetic field is used to investigate the possibility of phase transitions in hot (warm) nuclear matter, giving rise to droplet formation. Surface properties of asymmetric nuclear matter as the droplet surface energy and its thickness are also examined.

PACS number(s):21.65.+f, 21.90.+f,26.60.+c

1 Introduction

In heavy-ion collisions, part of the hot nuclear matter produced can be described in terms of hadrons. The formation of highly excited composed nuclei in equilibrium with a gas of evaporated particles can be interpreted in the framework of hydrodynamics as two coexisting phases of nuclear matter, a liquid and a gas phase [1]. During these reactions, phase transitions may occur depending on the temperature and densities involved [2]-[4]. The investigation of asymmetric nuclear matter is also of particular interest for problems in astrophysics. In fact, neutron-star matter at densities between 0.03 fm^{-3} and nuclear matter density (0.17 fm^{-3}) consists of neutron-rich nuclei immersed in a gas of neutrons [5]. The size of the nuclei is determined by a competition between the surface energy and the Coulomb interaction. The use of thermodynamical concepts in the study of possible phase transitions in the above problems is done with the underlying assumption that the time required for thermalization and chemical equilibrium is small.

Hot nuclei, liquid-gas phase transitions and droplet formation in nuclear reactions as well as the surface properties of nuclear matter have already been extensively discussed in the literature in the context of non–relativistic models, namely within the framework of the Hartree-Fock (HF), Thomas–Fermi(TF) and Extended–Thomas–Fermi approximations (ETF) [1],[6]- [10]. In particular, in [10] it is shown that the semi-classical TF approximation scheme is reasonably accurate at any temperature.

Within the framework of relativistic models phase transitions in hot (warm) nuclear matter have also been investigated in infinite matter by imposing constant mesonic fields [2], at zero temperature for symmetric semi-infinite nuclear matter [11], at finite temperature for symmetric matter in the linear Walecka model [3],[12] and also in its non–linear form for symmetric and asymmetric matter [13]. Surface properties of asymmetric semi–infinite nuclear matter have been investigated at zero temperature in [14] and [15] in terms of a semi–classical treatment. In most of the above mentioned papers in which temperature effects have been taken into account, the finite temperature version of the liquid drop model is used in the investigation of the surface properties of

the arising droplet.

In the present work, we study the possibility of droplet formation in a vapour system at finite temperature in the framework of the relativistic Walecka model with non linear terms (NLWM), which is known to describe adequately the bulk properties of nuclear matter. We include the Coulomb interaction and work in the Thomas-Fermi approximation. We determine the conditions for phase coexistence in a multi-component system by building the binodals for several temperatures and two parametrizations of the non-linear Walecka model. These values determine the initial conditions which are used in solving numerically the coupled equations of motion obtained in the Thomas-Fermi approximation at finite temperature. This semi-classical approximation contains the following quantal ingredients: the production of anti-particles is included and the distribution function of particles and anti-particles takes into account the Pauli Principle.

In section 2 we obtain the equations of motion in the static case. The thermodinamical potential in the framework of the Thomas-Fermi approximation is calculated in section 3. In section 4 the two–phase coexistence is discussed and in section 5 we present the numerical results. Finally, in the last section some conclusions are drawn.

2 Extended Non Linear Walecka Model

In what follows we describe the equation of state of non-symmetric matter within the framework of the relativistic non-linear Walecka model [16], [17] with the inclusion of ρ-mesons and the eletromagnetic field. The self interaction terms of the scalar meson were shown to be necessary in order to adequately describe nuclear properties [16]. Both the ρ meson and photons are incorporated to account, respectively, for the neutron excess in heavy nuclei and the eletromagnetic interaction between the protons [17]. In our lagrangian the π–meson field amplitude is not considered since we are not interested in pion–condensed states and hence, under the approximation we use here, all pion contributions vanish.

In this model the nucleons are coupled to neutral scalar ϕ, isoscalar-vector

V^μ, isovector-vector $\vec{b}^\mu$ meson fields and the electromagnetic field A^μ. The lagrangian density reads:

$$\begin{aligned}\mathcal{L} = \bar{\psi}\left[\gamma_\mu(i\partial^\mu - g_v V^\mu) - \frac{g_\rho}{2}\gamma_\mu\vec{\tau}\cdot\vec{b}^\mu - e\gamma_\mu A^\mu\frac{(1+\tau_3)}{2} - (M - g_s\phi)\right]\psi \\ +\frac{1}{2}(\partial_\mu\phi\partial^\mu\phi - m_s^2\phi^2) - \frac{1}{3!}\kappa\phi^3 - \frac{1}{4!}\lambda\phi^4 \\ -\frac{1}{4}\Omega_{\mu\nu}\Omega^{\mu\nu} + \frac{1}{2}m_v^2 V_\mu V^\mu + \frac{1}{4!}\xi g_v^4(V_\mu V^\mu)^2 \\ -\frac{1}{4}\vec{B}_{\mu\nu}\cdot\vec{B}^{\mu\nu} + \frac{1}{2}m_\rho^2\vec{b}_\mu\cdot\vec{b}^\mu - \frac{1}{4}F_{\mu\nu}F^{\mu\nu}\ , \end{aligned} \tag{1}$$

where

$$\Omega_{\mu\nu} = \partial_\mu V_\nu - \partial_\nu V_\mu, \tag{2}$$

$$\vec{B}_{\mu\nu} = \partial_\mu\vec{b}_\nu - \partial_\nu\vec{b}_\mu - g_\rho(\vec{b}_\mu\times\vec{b}_\nu), \tag{3}$$

and

$$F_{\mu\nu} = \partial_\mu A_\nu - \partial_\nu A_\mu. \tag{4}$$

The model comprises the following parameters: three coupling constants g_s, g_v and g_ρ of the mesons to the nucleons, the nucleon mass M, the masses of the mesons m_s, m_v, m_ρ, the eletromagnetic coupling constant $e = \sqrt{\frac{4\pi}{137}}$ and the self-interacting coupling constants κ, λ and ξ. We have used two sets of constants, respectively identified as MS taken from [2] and as NL1 taken from [22], with $C_i^2 = g_i^2 M^2/m_i^2$, $i = \ s,\ v,\ \rho$, and they are displayed in table 1. All meson masses must be specified along with the coupling constants. It is true that only the rations of couplings to the masses are necessary in infinite matter in the *linear* Walecka model. When non - linear terms are included, the statement looses its validity.

From the Euler–Lagrange formalism, we obtain the coupled equations of motion for the scalar, isoscalar-vector, isovector-vector, eletromagnetic and nucleon fields, respectively given by:

$$(\partial_t^2 - \nabla^2 + m_s^2)\phi = g_s\rho_s - \frac{\kappa}{2}\phi^2 - \frac{\lambda}{6}\phi^3, \tag{5}$$

$$(\partial_t^2 - \nabla^2 + m_v^2)V^\mu = g_v j^\mu - \frac{\xi}{6} g_v^4 (V^\mu)^3, \tag{6}$$

$$(\partial_t^2 - \nabla^2 + m_\rho^2)\vec{b}^\mu = \frac{g_\rho}{2}\vec{j}^\mu + \frac{g_\rho}{2}(\vec{b}_\nu \times \vec{B}^{\nu\mu}) + g_\rho \partial_\nu (\vec{b}^\nu \times \vec{b}^\mu), \tag{7}$$

$$(\partial_t^2 - \nabla^2)A^\mu = \frac{e}{2} j_{em}^\mu \tag{8}$$

and

$$i\partial_t \psi = \Bigg[\boldsymbol{\alpha} \cdot (-i\boldsymbol{\nabla} - g_v \mathbf{V} - \frac{g_\rho}{2}\tau_3 \mathbf{b} - e\frac{(1+\tau_3)}{2}\mathbf{A})$$

$$+\beta(M - g_s\phi) + g_v V^0 + \frac{g_\rho}{2}\tau_3 b^0 + e\frac{(1+\tau_3)}{2}A^0 \Bigg] \psi, \tag{9}$$

where the scalar density ρ_s and the baryonic current densities are defined as

$$\rho_s = < \bar{\psi}\psi >,$$

$$j^\mu = < \bar{\psi}\gamma^\mu \psi >,$$

$$\vec{j}^\mu = < \bar{\psi}\gamma^\mu \vec{\tau} \psi >,$$

$$j_{em}^\mu = < \bar{\psi}\gamma^\mu (\frac{1-\tau_3}{2})\psi >$$

and $b_3^\mu \equiv (b^0, \mathbf{b})$. In the static case there are no currents in the nucleus and the spatial vector components $\mathbf{V}$, $\mathbf{b}$ and $\mathbf{A}$ are zero. Therefore, the equations of motion become:

$$\nabla^2 \phi = m_s^2 \phi + \frac{1}{2}\kappa\phi^2 + \frac{1}{3!}\lambda\phi^3 - g_s\rho_s, \tag{10}$$

$$\nabla^2 V_0 = m_v^2 V_0 + \frac{1}{3!}\xi g_v^4 V_0^3 - g_v \rho_B, \tag{11}$$

$$\nabla^2 b_0 = m_\rho^2 b_0 - \frac{g_\rho}{2}\rho_3, \tag{12}$$

$$\nabla^2 A_0 = -e\rho_p, \tag{13}$$

where $\rho_B = \rho_p + \rho_n$ and $\rho_3 = \rho_p - \rho_n$ are the barionic densities, and ρ_p and ρ_n are the proton and neutron densities.

3 The Thomas–Fermi Approximation

The present work is based on the semi-classical Thomas-Fermi approximation. In this approach the energy of the nuclear system with particles and anti-particles, described respectively by the one-body phase-space distribution functions $n_+(\mathbf{r},\mathbf{p},t)$ and $n_-(\mathbf{r},\mathbf{p},t)$, at position $\mathbf{r}$ time t and with momentum $\mathbf{p}$

$$n_\pm(\mathbf{r},\mathbf{p},t) = \begin{pmatrix} n_{p\pm}(\mathbf{r},\mathbf{p},t) & 0 \\ 0 & n_{n\pm}(\mathbf{r},\mathbf{p},t) \end{pmatrix}, \tag{14}$$

is (only the nuclear matter contribution and interaction terms)

$$E_N \;=\; \gamma \mathrm{Tr} \int \frac{\mathrm{d}^3 r \mathrm{d}^3 p}{(2\pi)^3} \left(n_+(\mathbf{r},\mathbf{p},t)\epsilon_+ \; + n_-(\mathbf{r},\mathbf{p},t)\epsilon_- \right) \tag{15}$$

where

$$\epsilon_\pm = \begin{pmatrix} \epsilon_{p\pm} & 0 \\ 0 & \epsilon_{n\pm} \end{pmatrix}, \quad \epsilon_{i\pm} \;=\; \sqrt{(\mathbf{p} \mp \boldsymbol{\mathcal{V}}_i)^2 + (M - g_s\phi)^2} \pm \mathcal{V}_{i0}, \quad i = p, n,$$

with

$$\mathcal{V}_{p0} = g_v V_0 + \frac{g_\rho}{2} b_0 + eA_0 \;, \quad \mathcal{V}_{n0} = g_v V_0 - \frac{g_\rho}{2} b_0 \;,$$
$$\boldsymbol{\mathcal{V}}_p = g_v \mathbf{V} + g_\rho \mathbf{b} + e\mathbf{A} \;, \quad \boldsymbol{\mathcal{V}}_n = g_v \mathbf{V} - g_\rho \mathbf{b} \;,$$

are the classical effective one-body Hamiltonian for particles (+) and anti-particles (-) since particles and anti-particles have opposite baryonic charge and $\gamma = 2$ refers to the spin multiplicity. We can also work with the distribution function for particles at position $\mathbf{r}$, instant t with momentum $\mathbf{p}$, $f_+(\mathbf{r},\mathbf{p},t) = n_+(\mathbf{r},\mathbf{p},t)$ and the distribution function for antiparticles at position $\mathbf{r}$, instant t with momentum $-\mathbf{p}$, $f_-(\mathbf{r},\mathbf{p},t) = n_-(\mathbf{r},-\mathbf{p},t)$ so that

$$E_N \;=\; \gamma \mathrm{Tr} \int \frac{\mathrm{d}^3 r \mathrm{d}^3 p}{(2\pi)^3} \left(f_+(\mathbf{r},\mathbf{p},t)\; h_+ \; - f_-(\mathbf{r},\mathbf{p},t)\; h_- \right)$$

where

$$\begin{aligned} h_\pm \;&=\; \pm\epsilon_\pm(\mathbf{r},\pm\mathbf{p},t) \\ &=\; \begin{pmatrix} \pm\sqrt{(\mathbf{p} - \boldsymbol{\mathcal{V}}_p)^2 + (M - g_s\phi)^2} + \mathcal{V}_{p0} & 0 \\ 0 & \pm\sqrt{(\mathbf{p} - \boldsymbol{\mathcal{V}}_n)^2 + (M - g_s\phi)^2} + \mathcal{V}_{n0} \end{pmatrix}. \end{aligned}$$

The classical entropy of a Fermi gas is given by

$$S = -\gamma \sum_{i=p,n} \int \frac{\mathrm{d}^3 r d^3 p}{(2\pi)^3} \left(f_{i+} \ln \left(\frac{f_{i+}}{1-f_{i+}} \right) + \ln(1-f_{i+}) + (f_{i+} \leftrightarrow f_{i-}) \right) , \tag{16}$$

and the thermodynamic potencial is defined as

$$\Omega \; = \; E - TS - \sum_{i=p,n} \mu_i B_i, \tag{17}$$

where B_p , B_n are, respectively, the proton and the neutron number:

$$B_i \; = \; \int \mathrm{d}^3 r \rho_i(\mathbf{r}, t), \qquad \rho_i = \gamma \int \frac{\mathrm{d}^3 p}{(2\pi)^3} (f_{i+} - f_{i-}), \quad i = p, n \, , \tag{18}$$

μ_i is the chemical potential for particles of type i and T is the temperature. For a system in equilibrium, the distribution functions should be chosen to make the thermodynamic potencial Ω stationary and hence

$$f_{i\pm}(\mathbf{r}, \mathbf{p}, t) \; = \; \frac{1}{1 + \exp[(\epsilon \mp \nu_i)/T]} \, , \tag{19}$$

where $\nu_i \; = \mu_i - \mathcal{V}_{i0}$ is the effective chemical potential, $\epsilon = \sqrt{p^2 + M^*}$ and $M^* \; = \; M - g_s \phi$ is the effective nucleon mass. In the static approximation $\boldsymbol{\mathcal{V}}_{\pm} = 0$.

From the above expressions we get for (17)

$$\begin{aligned} \Omega = \; & \gamma \mathrm{Tr} \int \frac{\mathrm{d}^3 r \mathrm{d}^3 p}{(2\pi)^3} \left(f_+(\mathbf{r}, \mathbf{p}, t) h_+ \; - f_-(\mathbf{r}, \mathbf{p}, t) h_- \right) \\ & + \frac{1}{2} \int \mathrm{d}^3 r \left[(\nabla \phi)^2 - (\nabla V_0)^2 - (\nabla b_0)^2 - (\nabla A_0)^2 \right] \\ & + \frac{1}{2} \int \mathrm{d}^3 r \left[m_s^2 \phi^2 + \frac{2}{3!} \kappa \phi^3 + \frac{2}{4!} \lambda \phi^4 - m_v^2 V_0^2 - \frac{2}{4!} \xi g_v^4 V_0^4 - m_\rho^2 b_0^2 \right] \\ & - \gamma T \sum_i \int \mathrm{d}^3 r \frac{\mathrm{d}^3 p}{(2\pi)^3} \left[\frac{h_{i+}}{T} f_{i+} - \frac{h_{i-}}{T} f_{i-} + \ln(1 + e^{-(\epsilon - \nu_i)/T}) + \ln(1 + e^{-(\epsilon + \nu_i)/T}) \right] . \end{aligned} \tag{20}$$

Equation (20) can then be written in the form

$$\Omega = \int \mathrm{d}^3 r \left(\frac{1}{2} \left[(\nabla\phi)^2 - (\nabla V_0)^2 - (\nabla b_0)^2 - (\nabla A_0)^2 \right] - V_{ef} \right)$$

with

$$V_{ef} = -\frac{1}{2} \left[m_s^2 \phi^2 + \frac{2}{3!}\kappa\phi^3 + \frac{2}{4!}\lambda\phi^4 - m_v^2 V_0^2 - \frac{2}{4!}\xi g_v^4 V_0^4 - m_\rho^2 b_0^2 \right]$$

$$+\gamma T \sum_i \int \frac{\mathrm{d}^3 p}{(2\pi)^3} \left[\ln(1 + e^{-(\epsilon - \nu_i)/T}) + \ln(1 + e^{-(\epsilon + \nu_i)/T}) \right]. \qquad (21)$$

The fields that minimize Ω satisfy the equations

$$\frac{\partial V_{ef}}{\partial \phi} = -m_s^2 \phi - \frac{1}{2}\kappa\phi^2 - \frac{1}{3!}\lambda\phi^3 + g_s \rho_s, \qquad (22)$$

$$\frac{\partial V_{ef}}{\partial V_0} = m_v^2 V_0 + \frac{1}{3!}\xi g_v^4 V_0^3 - g_v \rho_B, \qquad (23)$$

$$\frac{\partial V_{ef}}{\partial b_0} = m_\rho^2 b_0 - \frac{g_\rho}{2}\rho_3, \qquad (24)$$

$$\frac{\partial V_{ef}}{\partial A_0} = -e\rho_p, \qquad (25)$$

where ρ_B, ρ_3 were defined at the end of section 2, ρ_p has been defined in (18) and

$$\rho_s = \gamma \sum_{i=p,n} \int \frac{\mathrm{d}^3 p}{(2\pi)^3} \frac{M^*}{\epsilon} \left(f_{i+} + f_{i-} \right).$$

Comparing eqs. (10–13) with eqs. (22–25), we see that

$$\nabla^2\phi = \frac{\mathrm{d}^2\phi}{\mathrm{d}r^2} + \frac{2}{r}\frac{\mathrm{d}\phi}{\mathrm{d}r} = -\frac{\partial V_{ef}}{\partial \phi}, \qquad (26)$$

$$\nabla^2 V_0 = \frac{\mathrm{d}^2 V_0}{\mathrm{d}r^2} + \frac{2}{r}\frac{\mathrm{d}V_0}{\mathrm{d}r} = \frac{\partial V_{ef}}{\partial V_0}, \qquad (27)$$

$$\nabla^2 b_0 = \frac{\mathrm{d}^2 b_0}{\mathrm{d}r^2} + \frac{2}{r}\frac{\mathrm{d}b_0}{\mathrm{d}r} = \frac{\partial V_{ef}}{\partial b_0}, \qquad (28)$$

$$\nabla^2 A_0 = \frac{\mathrm{d}^2 A_0}{\mathrm{d}r^2} + \frac{2}{r}\frac{\mathrm{d}A_0}{\mathrm{d}r} = \frac{\partial V_{ef}}{\partial A_0}. \qquad (29)$$

These coupled differential equations are solved numerically and all relevant quantities (e.g. effective mass, densities, pressure), which depend on the fields are calculated.

4 Two–phase coexistence

In order to obtain the initial conditions for the program which integrates the differential equations (26-29) we determine the conditions under which two distinct phases can coexist in infinite matter. In the mean field approximation the meson fields are replaced by their expectation values [2, 18],

$$\phi \equiv < \phi > = \phi_0, \tag{30}$$

$$V^0 \equiv < V^0 > = V_0, \tag{31}$$

$$b^0 \equiv < b^0 > = b_0, \tag{32}$$

and the eletromagnetic field vanishes. The substitution of the above expressions in eqs. (10), (11) and (12) yields

$$\phi_0 = -\frac{\kappa}{2m_s^2}\phi_0^2 - \frac{\lambda}{6}\phi_0^3 + \frac{g_s}{m_s^2}\rho_s, \tag{33}$$

$$V_0 = -\frac{\xi g_v^4}{6m_v^2}V_0^3 + \frac{g_v}{m_v^2}\rho_B, \tag{34}$$

$$b_0 = \frac{g_\rho}{2m_\rho^2}\rho_3. \tag{35}$$

The thermodynamic quantities of interest are given in terms of the above meson fields. They are the energy density:

$$\mathcal{E} = \frac{\gamma}{2\pi^2}\sum_{i=p,n}\int p^2 dp\sqrt{p^2 + M^{*2}}\,(f_{i+} + f_{i-})$$

$$+\frac{m_v^2}{2}V_0^2 + \frac{\xi g_v^4}{8}V_0^4 + \frac{g_\rho^2}{8m_\rho^2}\rho_3^2 + \frac{m_s^2}{2}\phi_0^2 + \frac{\kappa}{6}\phi_0^3 + \frac{\lambda}{24}\phi_0^4, \tag{36}$$

the pressure:

$$P = \frac{\gamma}{6\pi^2}\sum_{i=p,n}\int \frac{p^4 dp}{\sqrt{p^2 + M^{*2}}}\,(f_{i+} + f_{i-})$$

$$+\frac{m_v^2}{2}V_0^2+\frac{\xi g_v^4}{24}V_0^4+\frac{g_\rho^2}{8m_\rho^2}\rho_3^2-\frac{m_s^2}{2}\phi_0^2-\frac{\kappa}{6}\phi_0^3-\frac{\lambda}{24}\phi_0^4, \tag{37}$$

the entropy density:

$$\mathcal{S}=\frac{1}{T}(\mathcal{E}+P-\mu_p\rho_p-\mu_n\rho_n), \tag{38}$$

and the proton fraction:

$$Y_p=\frac{\rho_p}{\rho_B}. \tag{39}$$

A thorough study of the possibility of phase transitions in hot, asymmetric nuclear matter is done in [20] and [2]. In figure 1 we plot the pressure in terms of the baryonic density ρ_B for each proton fraction and for $T = 10$ MeV obtained with the MS constants. This figure is slightly different from figure 4 of [2], which is reproduced when $m_s = 500$ MeV. Similar behaviours are found for $T = 5$ MeV and also with the NL1 constants.

We have made use of the geometrical construction [20] in order to obtain the chemical potentials in the two coexisting phases for each pressure of interest. As an example, we show μ_p and μ_n in function of the proton fractions in figure 2 again for $T = 10$ MeV and MS constants.

In a binary system

$$\left(\frac{\partial\mu_p}{\partial Y_p}\right)_{T,P}\geq 0 \quad \text{and} \quad \left(\frac{\partial\mu_n}{\partial Y_p}\right)_{T,P}\leq 0, \tag{40}$$

known as diffusive stability, which reflects the fact that in a stable system, energy is required to change the proton concentration while pressure and temperature are kept constant. In order to obtain the binodal section which contains points under the same pressure for different proton fractions, we have used the conditions above and simultaneously solved the following equations:

$$P=P(\nu_p,\nu_n,M^*), \tag{41}$$

$$P=P(\nu_p',\nu_n',M^{*\prime}), \tag{42}$$

$$\mu_i(\nu_p,\nu_n,M^*)=\mu_i(\nu_p',\nu_n',M^{*\prime}) \quad ,i=p,n \tag{43}$$

$$\frac{m_s^2}{g_s^2}\phi_0 + \frac{\kappa}{2g_s^3}\phi_0^2 + \frac{\lambda}{6g_s^4}\phi_0^3 = \rho_s(\nu_p, \nu_n, M^*) \tag{44}$$

and

$$\frac{m_s^2}{g_s^2}\phi_0{}' + \frac{\kappa}{2g_s^3}\phi_0^{2\prime} + \frac{\lambda}{6g_s^4}\phi_0^{3\prime} = \rho_s(\nu_p', \nu_n', M^{*\prime}). \tag{45}$$

The binodal sections for the MS and the NL1 constants and temperatures equal to 5 and 10 MeV are plotted, respectively, in figure 3 and in figure 4. For certain values of proton and neutron chemical potentials, the system may be at the same pressure with different densities and proton concentrations, which allows for the possibility of phase transitions. For the sake of completeness, we also show in tables 2, 4 and 6 some of the points taken from the binodal sections. The results we have chosen as input to the code which solves the differential equations (26-29) are displayed in the last three columns of these tables.

5 Numerical Results

Solving numerically the set of coupled equations (26–29) is not trivial. The main problem is related with the boundary conditions which have to be set within the droplet. To understand better this statement, please refer to the Appendix, where the formulae are simplified to the $T = 0$ case and this problem becomes clear. At first, we have tried to use the code COLSYS [21], as suggested in [22] and [13], but we have obtained satisfactory results only for symmetric nuclear matter [23]. We have finally opted for another code, written with the help of the Gears stiff integration method, which uses as input the temperature, the size of the mesh, boundary conditions and initial conditions. The chemical potentials are output and can be *fitted* in accordance with the size of the mesh. In the Appendix the boundary and initial conditions we have used are explicitly written.

The radius R_{max} (see Appendix) fixes the neutron chemical potential calculated at the last mesh point. The proton chemical potential is fixed by another (inner) mesh point, which depends on the difference desired between both potentials. If $\mu_p = \mu_n$ (symmetric nuclear matter), R_{max} fixes both chemical

potentials at the last mesh point. We have considered that convergence has been achieved when the baryonic density does not vary more than 0.5 per cent and the chemical potentials are close to the ones obtained from the binodal section for a certain proton fraction.

As an example, in figure 5 we plot the fields which are solutions of the coupled equations for the MS parametrization at T=10 MeV with the initial conditions given in table 2 for $Y_p = 0.3$. The corresponding barionic density is plotted in figure 6 and represents a droplet of the liquid phase (small r) in the background of the vapour phase (large r). Similar density profiles are obtained for all other proton fractions, except for $Y_p = 0.5$, when the curves for proton and neutron densities coincide. The region at the surface with extra neutrons is known as *neutron skin*. Some quantities of interest to study the surface properties are the two *squared–off* radii R_n and R_p, defined in [6] as

$$\int_0^{R_{max}} \rho_n(r)\mathrm{d}r = \rho_{n,i}R_n + \rho_{n,f}(R_{max} - R_n), \tag{46}$$

and

$$\int_0^{R_{max}} \rho_p(r)\mathrm{d}r = \rho_{p,i}R_p + \rho_{p,f}(R_{max} - R_p), \tag{47}$$

where ρ_i refers to the liquid density, ρ_f to the gas density, R_{max} is the size of the mesh for which convergence is achieved, and the neutron skin thickness [15]

$$\Theta = R_n - R_p. \tag{48}$$

These quantities are computed for the droplet solutions we obtain and given in tables 3, 5, 7.

The droplet surface energy and thickness are obtained from the free energy of a system with a fixed number of particles $B = B_p + B_n$, in which a droplet of arbitrary size grows in the background of the vapour phase. Within the small surface thickness approximation it reads [12]:

$$F = \int 4\pi r^2 \mathrm{d}r \left[\left(\frac{\mathrm{d}\phi}{\mathrm{d}r}\right)^2 - \left(\frac{\mathrm{d}V_0}{\mathrm{d}r}\right)^2 - \left(\frac{\mathrm{d}b_0}{\mathrm{d}r}\right)^2 - \left(\frac{\mathrm{d}A_0}{\mathrm{d}r}\right)^2 - C \right] + \mu_p B_p + \mu_n B_n. \tag{49}$$

For droplets with radius R and small surface thickness,

$$F(R) = 4\pi\sigma R^2 - CV + \mu_p B_p + \mu_n B_n, \tag{50}$$

where C is a constant and V is the volume of the system. The surface energy per unit area of these droplets is

$$\sigma = \int_0^\infty \mathrm{d}r \left[\left(\frac{\mathrm{d}\phi}{\mathrm{d}r} \right)^2 - \left(\frac{\mathrm{d}V_0}{\mathrm{d}r} \right)^2 - \left(\frac{\mathrm{d}b_0}{\mathrm{d}r} \right)^2 - \left(\frac{\mathrm{d}A_0}{\mathrm{d}r} \right)^2 \right]. \tag{51}$$

The surface thickness t is defined as the width of the region where the density drops from $0.9\rho_{B0}$ to $0.1\rho_{B0}$, where ρ_{B0} is the baryonic density at $r = 0$. According to [16], for $T = 0$, σ should be of the order of 1.25 MeV fm^{-2} and t of the order of 2.2 fm.

In table 2 some points taken from the binodal section for the MS constants at $T = 10$ MeV are explicitly written. In table 3 results found for the proton fractions at $r = 0$ ($Y_p(i)$), chemical potentials, the surface energy, its thickness, the size of the mesh for which convergence is achieved, R_{max}, R_p and the neutron skin thickness are displayed. Notice that there is a small discrepancy between the proton and neutron chemical potentials given in table 2 and the ones displayed in table 3. This is due to finite size effects and the inclusion of the Coulomb interaction. In tables 4 and 5 again the points obtained from the binodal section at $T = 5$ MeV and the respective droplet solutions are shown for the MS set of constants while in tables 6 and 7 the NL1 constants are used.

At this point some comments are in order. The size of the mesh (R_{max}) given in tables 3, 5 and 7 are the smaller values for which there is convergence for a given density at $r = 0$ and a given proton fraction Y_p within the accuracy of the present numerical calculations, i.e., $\pm 0.5\%$. We have chosen to compare data corresponding to the same value of the proton fraction at $r = 0$ because this parameter is independent of the propeties of the surface. A larger mesh size would converge to a larger droplet with the same values for the proton fraction Y_p and the density at $r = 0$, and the same chemical potentials. For a detailed explanation on the introduction of the Coulomb field, please refer to the Appendix. Before drawing our conclusions, we would like to emphasize that in our calculations, the proton and neutron numbers are never fixed. They

are just consequence of the results for the fields and densities obtained from the convergent solutions of the differential equations.

6 Conclusions

We first examine the behaviour of the total baryonic density. From figure 6, one can see that it falls from the initial liquid density to the vapour density, which is very small, but different from zero, as expected. One can compare this figure with the densities presented in table 2 for infinite nuclear matter with $Y_p = 0.3$. Concerning the neutron and proton densities, figure 6 shows the same profile obtained in [10] and [6] with non–relativistic models.

The proton fraction in the vapour phase is smaller than in the liquid phase ($Y_p(i)$), except for the symmetric nuclear matter, when it remains unaltered. This can be seen from tables 2, 4 and 6 and confirmed for the droplet solutions. This fact can be interpreted as a nucleus with a given proton concentration (the phase of higher density) in equilibrium with a gas of drip nucleons, mostly neutrons (the lower density phase) with a much smaller proton concentration.

From tables 3, 5 and 7, one can check that the surface energy σ increases with the initial proton fraction and its thickness t decreases. In fact, the larger the proton fraction the less important is the contribution from the b_0 field in the σ calculation as can be seen from (51). For symmetric nuclear matter, the results are compatible with the ones suggested in [16] and for asymmetric matter the surface thickness results are comparable with the ones presented in [15]. One can also see that the larger the proton fraction, the smaller the size of the mesh for which convergence is achieved. This may be due to the decrease of neutron–proton asymmetry and therefore, the increase of the droplet binding. Some conclusions with respect to the temperature dependence of the droplet solutions can be drawn comparing tables 3 and 5. First, it is easy to note that the size of the mesh must be larger for higher temperatures. A similar statement was made in [13]. Also, the surface energy decreases with the increase of temperature, while the surface thickness is larger for higher temperatures. The decrease of σ with the temperature is easily understood from (51), because for higher temperatures the fields decrease more

smoothly and spread out over a larger distance at the surface and, therefore, their derivatives are smaller.

In the same tables the squared-off proton radius and the neutron skin thickness are also shown. Both quantities decrease with the increase of the proton fraction at $r = 0$. The numbers we have obtained can be compared with the ones found in [6]. These behaviours could be a consequence of the increase of the droplet binding. The neutron skin thickness is a quantity which is larger for lower temperatures, except for symmetric nuclear matter, when it is zero, independently of the temperature considered.

Concerning the importance of the Coulomb interaction and its consequences in the droplet formation, one can see, from figure 6, that the proton and neutron densities are indeed modified by the eletromagnetic field, as pointed out in [1]. Nevertheless, for the same value of Y_p at $r = 0$, the profile of the surface with eletromagnetic field is almost unaltered with respect to the results obtained without the Coulomb interaction. This fact is reflected in the results displayed in table 3.a, which were obtained with the same input parameters as the ones shown in the third line of table 3, but without the inclusion of the eletromagnetic interaction. The surface energy σ, the proton radius R_p and the neutron skin Θ are slightly different when they are calculated with and without the Coulomb potential while t is practically the same. Two effects of the eletromagnetic field in the present calculation is to decrease the number of particles in the droplet, since the central density becomes smaller, and to increase the proton radius R_p.

The conclusions drawn above are independent of the sets of parameters used.

To the best of our knowledge, this is the first time that the eletromagnetic interaction is taken into account within the framework of a relativistic model in order to calculate surface properties. We believe that a more systematic study of the importance of the Coulomb field for various temperatures and proton fractions has still to be made and this problem will be tackled in a forthcoming work.

Appendix

For $T = 0$ the distribution functions are simply given by:

$$f_i = \theta(k_{Fi}^2(r) - p^2), \qquad i = p, n$$

and, hence,

$$h_i = h_{i+},$$

$$\begin{aligned} V_{ef} &= -\frac{1}{2}\left[m_s^2\phi^2 + \frac{2}{3!}\kappa\phi^3 + \frac{2}{4!}\lambda\phi^4 - m_v^2 V_0^2 - \frac{2}{4!}\xi g_v^4 V_0^4 - m_\rho^2 b_0^2\right] \\ &\quad -\gamma\sum_{i=p,n}\int\frac{\mathrm{d}^3p}{(2\pi)^3}h_i f_i + \mu_p\rho_p + \mu_n\rho_n, \end{aligned}$$

$$\rho_s = \gamma\sum_{i=p,n}\int\frac{\mathrm{d}^3p}{(2\pi)^3}\frac{M^*}{\epsilon}f_i = \frac{\gamma}{2\pi^2}\sum_{i=p,n}\int_0^{k_{Fi}(r)} p^2\mathrm{d}p\frac{M^*}{\epsilon},$$

$$\rho_i = \gamma\int\frac{\mathrm{d}^3p}{(2\pi)^3}f_i = \frac{\gamma}{6\pi^2}k_{Fi}^3(r).$$

Minimization of Ω with respect to $k_{Fi}(r)$, $i = p, n$, gives rise to the following conditions

$$k_{Fp}^2(r)\left(\mu_p - \sqrt{k_{Fp}^2(r) + {M^*}^2(r)} - g_v V_0 - \frac{g_\rho}{2}b_0 - eA_0\right) = 0$$

and

$$k_{Fn}^2(r)\left(\mu_n - \sqrt{k_{Fn}^2(r) + {M^*}^2(r)} - g_v V_0 + \frac{g_\rho}{2}b_0\right) = 0.$$

We obtain $k_{Fp}(r) = 0$ and $k_{Fn}(r) = 0$ or, for $k_{Fp}(r)$ and $k_{Fn}(r)$ different from zero,

$$\mu_p = \sqrt{k_{Fp}^2(r) + {M^*}^2(r)} + g_v V_0 + g_\rho b_0 + eA_0, \tag{52}$$

$$\mu_n = \sqrt{k_{Fn}^2(r) + {M^*}^2(r)} + g_v V_0 - g_\rho b_0. \tag{53}$$

The value of $k_{Fp}(r)$ and $k_{Fn}(r)$ is obtained inverting these last two equations. The discontinuity on the values of $k_{Fp}(r)$ and $k_{Fn}(r)$ has to be taken into account in the code that solves the differential equations (22–25). Outside the droplet $k_{Fp}(r)$ and $k_{Fn}(r)$ are zero and the mesons are free.

In our code, the boundary conditions are given by

$$\frac{\mathrm{d}\phi}{\mathrm{d}r}(r=0) = \frac{\mathrm{d}V_0}{\mathrm{d}r}(r=0) = \frac{\mathrm{d}b_0}{\mathrm{d}r}(r=0) = \frac{\mathrm{d}A_0}{\mathrm{d}r}(r=0) = 0$$

and for $r = R_{max}$, where R_{max} is the size of the mesh,

$$\frac{\mathrm{d}\phi}{\mathrm{d}r} + (m_s + \frac{1}{R_{max}})\phi = 0,$$

with similar equations for V_0 and b_0 and

$$\frac{\mathrm{d}A_0}{\mathrm{d}r} + \frac{A_0}{R_{max}} = 0,$$

or, considering the electron screening, A_0 is zero at the last point of the mesh,

$$A_0(R_{max}) = 0.$$

Both boundary conditions give similar results.

As initial guesses for the meson fields we have used Fermi like functions such as

$$\phi(r) = \frac{\phi_0}{1 + \exp(m_s(r - 0.8R_{max}))},$$

for the scalar field. The values for $r = 0$, i.e. ϕ_0, V_{00} and b_0 were obtained from the binodal section. An initial guess for the eletromagnetic field is the field of a homogeneous spherical distribution of protons which at $r = 0$ is of the order of 1×10^{-2} in units of nucleon mass. The convergence is obtained for different initial guesses except if the initial guesses are much stronger than the value refered above. We also suppose that the droplets are formed in an electrically neutral enviroment, as we would find in neutron stars.

Acknowledgements

We would like to thank Dr. Manuel Fiolhais for helping us with the COLSYS code, Dr. Hans Walliser for giving us his fortran code which solves the differential equations and for his useful suggestions and Dr. J. da Providência for his comments. One of the authors (DPM) would like to acknowledge the warm hospitality of the Centro de Física Teórica of the University of Coimbra, where this work was acomplished. This work has been partially supported by Capes - Brazil.

References

[1] P. Bonche, S. Levit and D. Vautherin, Nucl. Phys. A427 (1984) 278; Nucl. Phys. A436 (1985) 265.

[2] H. Müller and B.D. Serot, Phys. Rev. C 52 (1995) 2072.

[3] H. Reinhardt and H. Schulz, Nucl. Phys. A432 (1985) 630.

[4] A.H. Blin, B. Hiller, H. Reinhardt and P. Schuck, Nucl. Phys. A484 (1988) 295.

[5] S.L. Shapiro and S.A. Teukolsky, *Black Holes, White Dwarfs and Neutron Stars*, John Wiley & Sons, N.Y., 1983; C.J. Pethick, D.G. Ravenhall, C.P. Lorenz, Nucl. Phys. A 584 (1995) 675.

[6] D.G. Ravenhall, C.J. Pethick and J.M. Lattimer, Nucl. Phys. A407 (1983) 571; G. Baym, H.A. Bethe and C.J. Pethick, Nucl. Phys. A 175 (1971) 225; D.G. Ravenhall, C. D. Bennet and C.J. Pethick, Phys. Rev. Lett. 28 (1972)978

[7] A.L. Goodman, J.I. Kapusta and A.Z. Mekjian, Phys. Rev. C 30 (1984) 851.

[8] K. Kolehmainen, M. Prakash, J.M. Lattimer and J.R. Treiner, Nucl. Phys. A 439 (1985) 535.

[9] W.D. Myers, W.J. Swiatecki and C.S. Wang, Nucl. Phys. A 436 (1985) 185.

[10] E. Suraud, Nucl. Phys. A 462 (1987) 109.

[11] F.J.B. Salzedas, MSc. Dissertation - Universidade de Coimbra - 1995

[12] M. Nielsen and J. Providência, J. Phys. G 16 (1990) 649.

[13] H. Müller and R.M. Dreizler, Nucl. Phys. A 563 (1993) 649.

[14] D. Von Eiff, J. M. Pearson, W. Stocker and M. K.Weigel, Phys. Lett. B 324 (1994) 279.

[15] M. Centelles, M. Del Estal and X. Viñas, preprint, 1997.

[16] J. Boguta and A. R. Bodmer, Nucl. Phys. A292, (1977) 413; A.R. Bodmer and C.E. Price, Nucl. Phys. A505 (1989) 123; A.R. Bodmer, Nucl. Phys. A526 (1991) 703.

[17] Y.K. Gambir, P. Ring, A. Thimet, Ann. Phys. 198 (1990) 132; H. Berghammer, D. Vretenar and P. Ring, Phys. Lett. B 296 (1992) 290; D. Vretenar, H. Berghammer and P. Ring, Phys. Lett. B 319 (1993) 29; H. Berghammer, D. Vretenar and P. Ring, Nucl. Phys. A 560 (1993) 1014.

[18] Sumiyoshi and Toki, Astroph. J. 422 (1944) 700.

[19] B.D. Serot and J.D. Walecka, Adv. Nucl. Phys. 16 (1995) 1.

[20] M. Barranco and J.R. Buchler, Phys. Rev. C 22 (1980) 1729.

[21] U. Asher, J. Christiansen and R.D. Russell, Math. Comput. 33 (1979) 659; U. Asher, J. Comput. Phys. 34 (1980); G. Bader and U. Asher, SIAM, J. Sci. Stat. Comput. 8 (1987) 483.

[22] C. Speicher, E. Engel and R.M. Dreizler, Nucl. Phys. A562 (1993) 569.

[23] M. Centelles, X. Vinãs, M. Barranco, S. Marcos and R.J. Lombard, Nucl. Phys. A537 (1992) 486.

7 Figure Captions

- **Figure 1.** The pressure in terms of the baryonic density is plotted for each proton fraction for the MS set of constants. The first curve on the left relates to $Y_p = 0$, the second one to $Y_p = 0.1$,..., the last one to $Y_p = 0.5$. The temperature is $T = 10$ MeV. The pressure is given in MeV/fm^3 and the density in fm^{-3}.

- **Figure 2.** The proton (lower curve) and the neutron (upper curve) chemical potentials are shown in function of the proton fraction for the pressure of 0.12 MeV/fm^3. Again this graph is plotted for MS constants and $T = 10$ MeV.

- **Figure 3.** Binodal section for $T = 10$ (dashed line) and $T = 5$ MeV (solid line) with the MS constants. The pressure is given in MeV/fm^3.

- **Figure 4.** Binodal section for $T = 10$ (dashed line) and $T = 5$ MeV (solid line) with the NL1 constants. The pressure is given in MeV/fm^3.

- **Figure 5.** ϕ,V_0,A_0 and b_0 (in this order, from top to bottom) are shown in terms of r. The fields are given in nucleon mass units and are obtained with the input values of table 2 for $Y_p = 0.3$.

- **Figure 6.** From top to bottom the density profiles for the baryons $\rho_B(r)$, the neutrons $\rho_n(r)$ and the protons $\rho_p(r)$ in fm^{-3} are plotted for the same case as in Fig. 5. The solid curves were obtained with the inclusion of the eletromagnetic field and the dashed ones without it.

8 Table Captions

- **Table 1.** Sets of parameters used in this work. All masses are given in MeV. The * is a reminder that the authors of [2] use a different scalar meson mass.

- **Table 2.** Results obtained from the binodal section built with the MS constants for $T = 10$ MeV. The pressures are given in MeV/fm^3, the

densities in fm^{-3}, the chemical potentials in MeV and the fields in units of nucleon mass.

- **Table 3.** Output results given by the solution of the coupled differential equations with the MS constants and $T = 10$ MeV. Index i refers to $r = 0$. The effective chemical potentials are given in units of nucleon mass, the chemical potentials in MeV, the surface energy in MeV/fm^2 and the surface thickness in fm. R_{max} is the size of the mesh for which convergence is achieved and it is given in fm. R_p and Θ are also given in fm.

- **Table 3.a** Output results given by the solution of the coupled differential equations with the MS constants and $T = 10$ MeV without the inclusion of the eletromagnetic field. The units are the same as in Table 3.

- **Table 4.** Results obtained from the binodal section built with the MS constants for $T = 5$ MeV. The units are the same as in Table 2.

- **Table 5.** Output results given by the solution of the coupled differential equations with the MS constants and $T = 5$ MeV. The units are the same as in Table 3.

- **Table 6.** Results obtained from the binodal section built with the NL1 constants for $T = 5$ MeV. The units are the same as in Table 2.

- **Table 7.** Output results given by the solution of the coupled differential equations with the NL1 constants and $T = 5$ MeV. The units are the same as in Table 3.

Table 1 - parameters

Force	[ref]	C_s^2	C_v^2	C_ρ^2	$\kappa/M \times 10^{-3}$	$\lambda \times 10^{-3}$	ξ	M	m_s	m_v	m_ρ
MS	[1]	374.770	260.570	106.91	3.0809×10^3	8.106×10^3	0.02364	939.	550.00*	783.00	770.00
NL1	[12]	373.176	245.458	149.67	$2\ g_s^3$ 2.4578	- $6\ g_s^4$ 3.4334	0.0	938.	492.25	795.36	763.00

Table 2

Y_p	$\mathcal{P}$	μ_p	μ_n	ρ_B	$\phi_0 \times 10^{-2}$	$V_{00} \times 10^{-2}$	$b_0 \times 10^{-2}$
0.10	0.38	873.90	941.36	0.08	2.01	1.30	-0.35
0.18				0.10	2.69	1.76	-0.39
0.20	0.35	874.66	940.86	0.11	2.82	1.85	-0.38
0.08				0.07	1.82	1.17	-0.33
0.25	0.27	877.55	939.04	0.13	3.15	2.07	-0.36
0.05				0.05	1.35	0.85	-0.25
0.30	0.18	882.16	936.42	0.14	3.44	2.28	-0.33
0.03				0.03	0.83	0.51	-0.16
0.35	0.10	888.56	932.55	0.15	3.69	2.44	-0.26
0.03				0.01	0.41	0.25	-0.08
0.40	0.06	896.36	927.37	0.16	3.87	2.57	-0.19
0.06				0.01	0.21	0.12	-0.04
0.45	0.03	904.90	920.77	0.17	3.98	2.64	-0.10
0.19				$4. \times 10^{-3}$	0.11	0.07	-0.01
0.50	0.03	913.20	913.18	0.17	4.01	2.67	-1.0×10^{-4}
0.50				$3. \times 10^{-3}$	0.09	0.05	-0.1×10^{-4}

Table 3

$Y_p(i)$	$\nu_p(i)$	$\nu_n(i)$	μ_p	μ_n	σ	t	R_{max}	R_p	Θ
0.15	0.75170	0.78836	876.18	935.30	0.22	5.03	16.70	12.46	0.75
0.23	0.70667	0.73960	879.62	935.25	0.35	4.72	15.73	11.63	0.71
0.30	0.66064	0.68956	884.29	933.99	0.58	3.36	10.49	7.50	0.59
0.36	0.62472	0.64845	892.46	932.22	0.70	3.21	9.44	6.75	0.47
0.38	0.61380	0.63467	896.94	931.08	0.76	3.02	8.39	5.96	0.38
0.50	0.61306	0.61328	913.20	913.20	1.21	2.46	7.34	3.72	0.0

Table 3.a

$Y_p(i)$	$\nu_p(i)$	$\nu_n(i)$	μ_p	μ_n	σ	t	R_{max}	R_p	Θ
0.30	0.65717	0.68534	882.72	933.99	0.60	3.36	10.49	7.39	0.62

Table 4

Y_p	$\mathcal{P}$	μ_p	μ_n	ρ_B	$\phi_0 \times 10^{-2}$	$V_{00} \times 10^{-2}$	$b_0 \times 10^{-2}$
0.15	0.52	868.12	948.93	0.12	3.01	1.97	-0.48
0.05				0.09	2.28	1.48	-0.45
0.20	0.37	871.18	946.76	0.13	3.26	2.15	-0.46
0.02				0.07	1.92	1.23	-0.39
0.25	0.19	875.63	943.75	0.14	3.49	2.31	-0.41
$6. \times 10^{-3}$				0.05	1.46	0.93	-0.30
0.30	0.06	881.47	940.25	0.15	3.73	2.47	-0.36
$2. \times 10^{-4}$				0.02	0.62	0.38	-0.12
0.35	0.02	888.80	936.36	0.17	3.96	2.63	-0.29
$2. \times 10^{-4}$				$4. \times 10^{-3}$	0.13	0.08	-0.03
0.40	6.	897.55	930.92	0.18	4.12	2.74	-0.20
$2. \times 10^{-3}$	$\times 10^{-3}$			$1. \times 10^{-3}$	0.04	0.02	-0.01
0.45	1.	906.87	924.01	0.18	4.22	2.81	-0.10
0.03	$\times 10^{-3}$			$3. \times 10^{-4}$	0.01	0.01	$-2. \times 10^{-3}$
0.50	5.	915.82	915.89	0.18	4.25	2.83	0.0
0.50	$\times 10^{-4}$			$1. \times 10^{-4}$	$3. \times 10^{-3}$	$2. \times 10^{-3}$	0.0

Table 5

$Y_p(i)$	$\nu_p(i)$	$\nu_n(i)$	μ_p	μ_n	σ	t	R_{max}	R_p	Θ
0.10	0.75486	0.79229	873.60	936.92	0.22	3.27	12.59	8.63	1.16
0.22	0.70784	0.73992	879.47	936.02	0.42	2.94	10.49	7.02	0.98
0.28	0.67424	0.70386	882.57	935.11	0.58	2.77	9.23	6.15	0.81
0.38	0.91239	0.63308	899.08	934.24	0.92	2.49	7.34	4.74	0.50
0.50	0.59357	0.59381	915.80	915.80	1.35	2.33	5.24	3.69	0.0

Table 6

Y_p	$\mathcal{P}$	μ_p	μ_n	ρ_B	$\phi_0 \times 10^{-2}$	$V_{00} \times 10^{-2}$	$b_0 \times 10^{-2}$
0.10	0.29	885.36	946.59	0.07	1.90	1.11	-0.35
0.11				0.06	1.82	1.06	-0.34
0.15	0.27	885.91	946.13	0.07	2.10	1.24	-0.35
0.07				0.05	1.61	0.92	-0.32
0.20	0.24	886.59	945.65	0.09	2.43	1.45	-0.35
0.06				0.05	1.51	0.86	-0.31
0.25	0.18	888.97	944.02	0.10	2.73	1.64	-0.33
0.03				0.04	1.23	0.69	-0.26
0.30	0.10	892.61	941.56	0.11	3.02	1.83	-0.30
0.01				0.03	0.85	0.47	-0.19
0.35	0.04	897.60	938.35	0.12	3.35	2.05	-0.25
$3. \times 10^{-3}$				0.01	0.36	0.19	-0.08
0.40	0.01	904.32	933.97	0.13	3.67	2.26	-0.18
$5. \times 10^{-3}$				$3. \times 10^{-3}$	0.10	0.05	-0.02
0.45	4.	912.06	928.06	0.14	3.89	2.40	-0.10
0.05	$\times 10^{-3}$			$8. \times 10^{-4}$	0.03	0.01	$-5. \times 10^{-3}$
0.50	1.65	920.42	920.46	0.14	3.97	2.45	$-2. \times 10^{-4}$
0.50	$\times 10^{-3}$			$3. \times 10^{-4}$	0.01	0.01	0.0

Table 7

$Y_p(i)$	$\nu_p(i)$	$\nu_n(i)$	μ_p	μ_n	σ	t	R_{max}	R_p	Θ
0.15	0.81150	0.83765	885.55	937.21	0.21	3.55	13.64	9.56	1.02
0.24	0.77241	0.79539	889.32	936.84	0.34	3.27	12.59	8.84	0.86
0.32	0.72522	0.74488	895.33	936.27	0.56	3.00	11.54	8.26	0.64
0.38	0.68604	0.70168	902.60	934.54	0.81	2.65	9.44	6.80	0.44
0.42	0.65833	0.67021	909.25	932.60	1.00	2.51	8.39	6.15	0.28
0.45	0.63661	0.64454	914.91	929.43	1.17	2.50	7.34	5.45	0.15

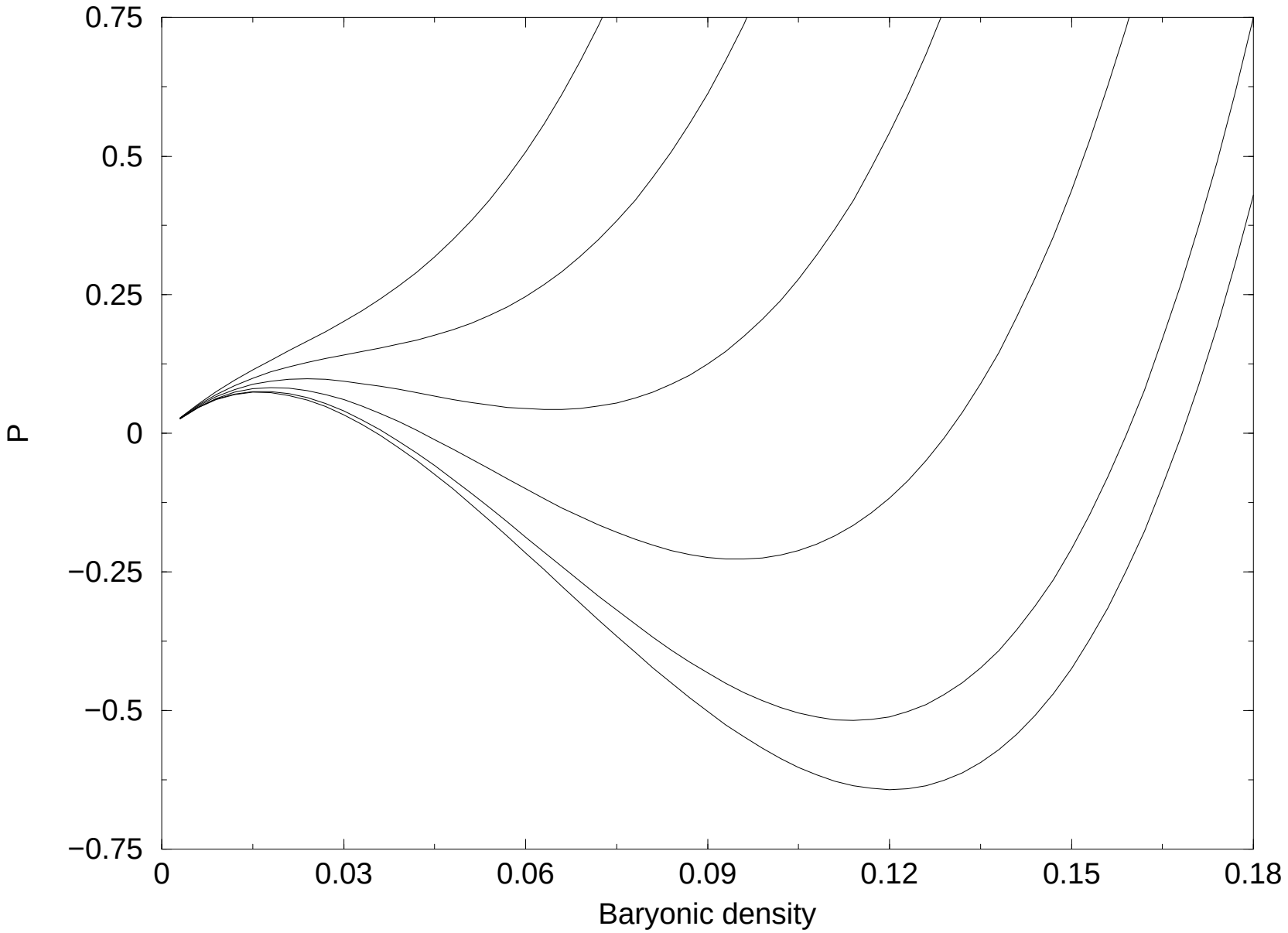
0.75
0.5
0.25
0
−0.25
−0.5
−0.75
P
0
0.03
0.06
0.09
0.12
0.15
0.18
Baryonic density

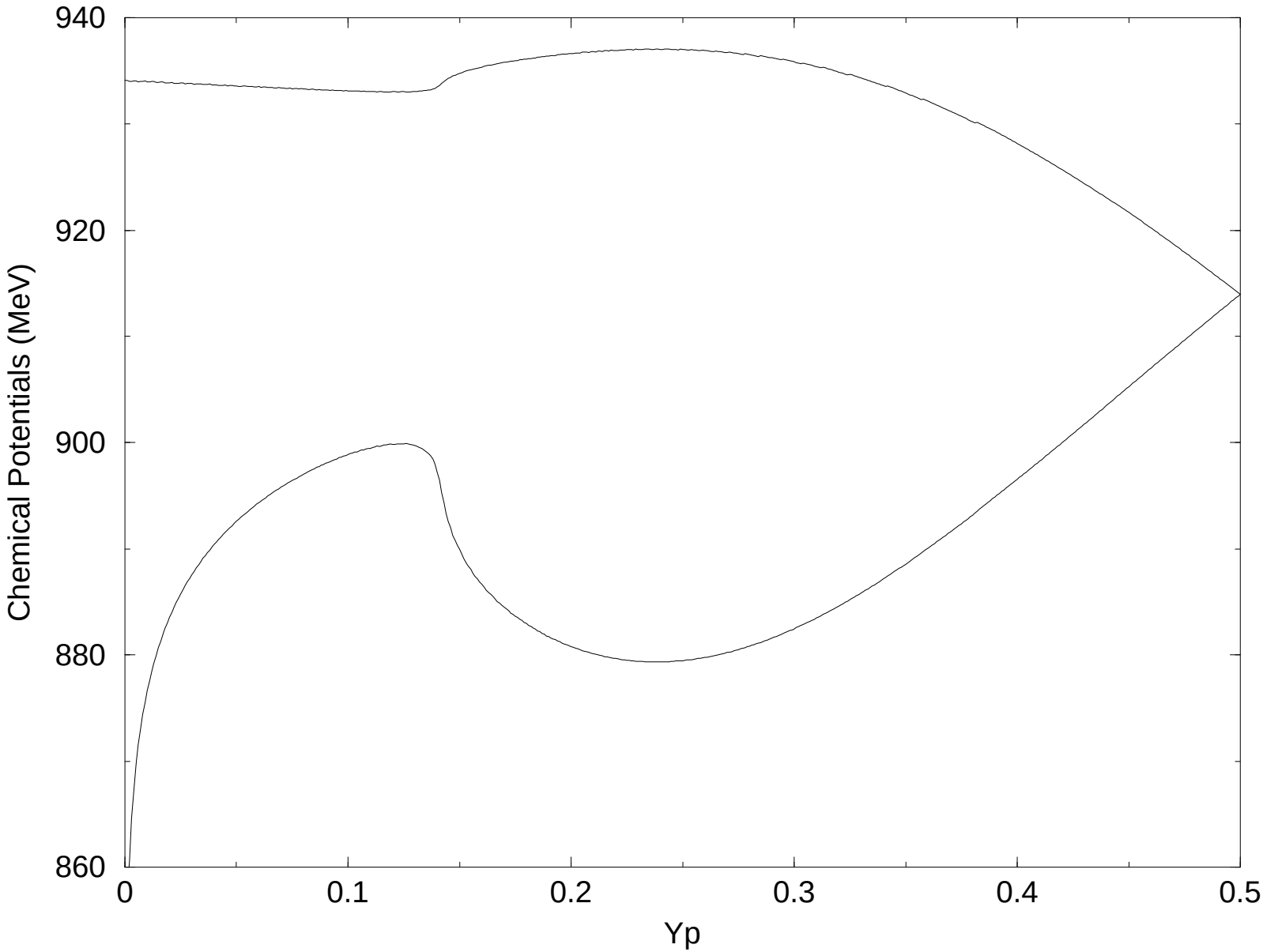
940
920
900
880
860
Chemical Potentials (MeV)
0
0.1
0.2
0.3
0.4
0.5
Yp

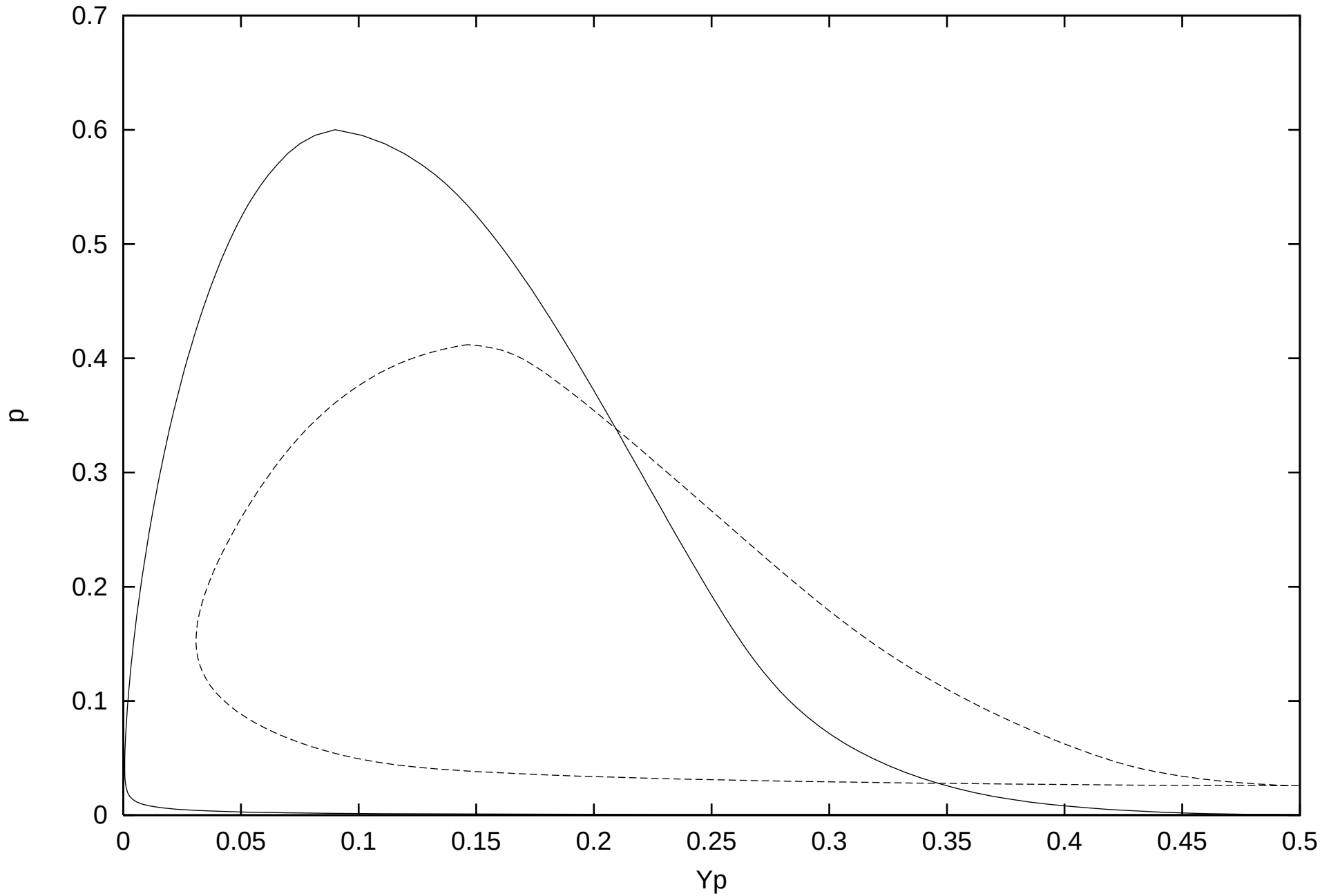
0.7
0.6
0.5
0.4
0.3
0.2
0.1
0
p
0
0.05
0.1
0.15
0.2
0.25
0.3
0.35
0.4
0.45
0.5
Yp

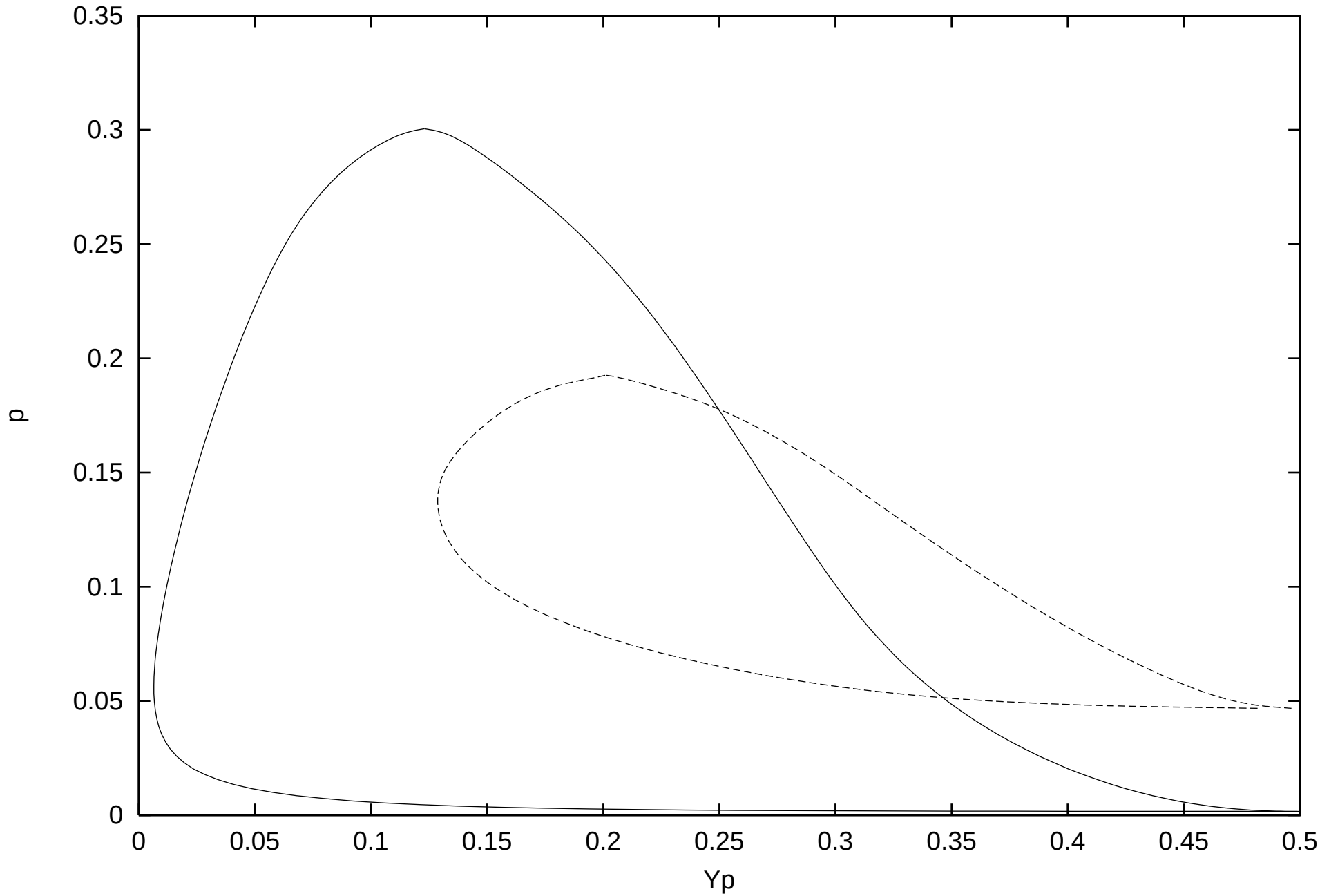
0.35
0.3
0.25
0.2
0.15
0.1
0.05
0
p
0
0.05
0.1
0.15
0.2
0.25
0.3
0.35
0.4
0.45
0.5
Yp

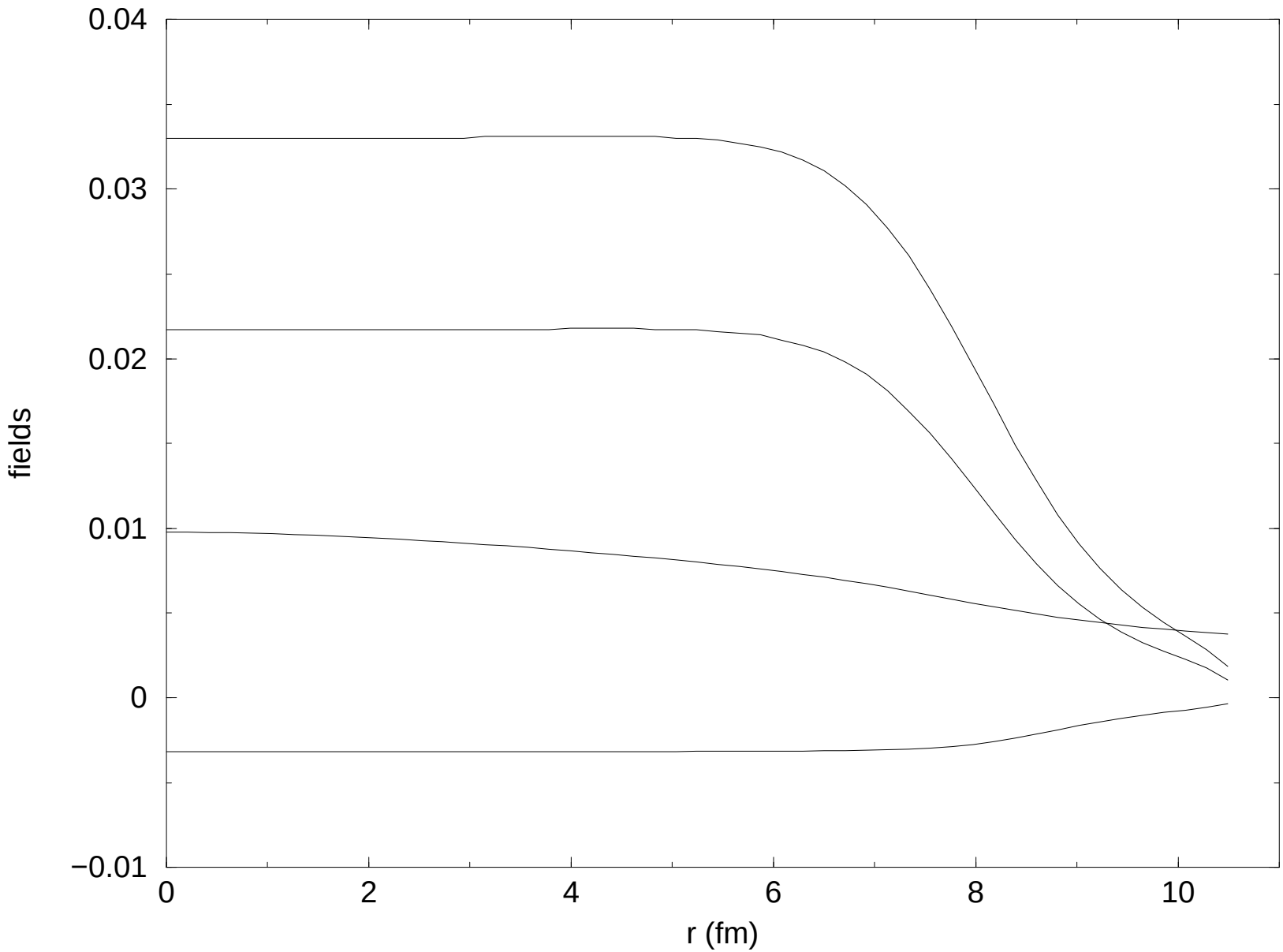
0.04
0.03
0.02
0.01
0
−0.01
fields
0
2
4
6
8
10
r (fm)

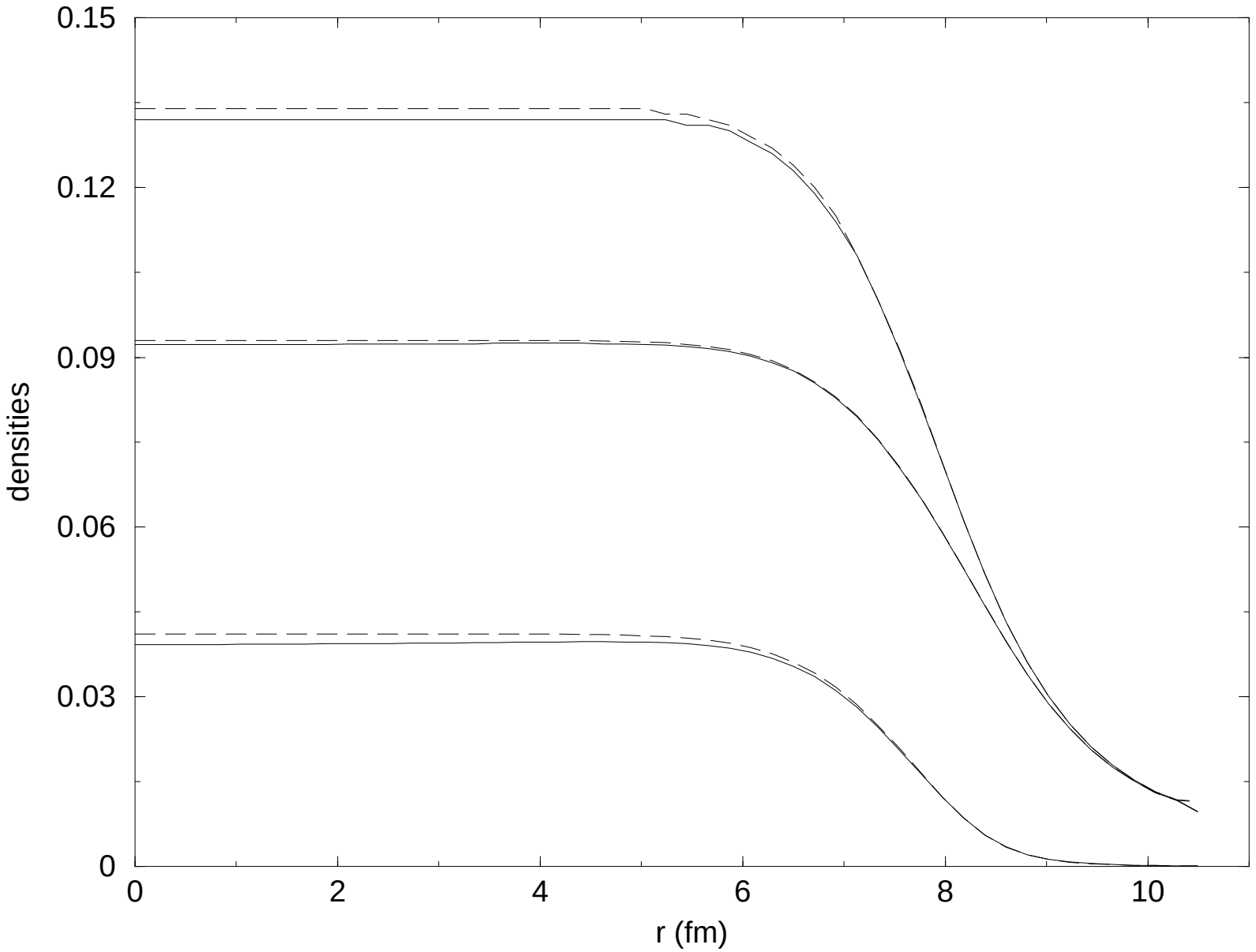
0.15
0.12
0.09
0.06
0.03
0
densities
0
2
4
6
8
10
r (fm)